A&A 604, A27 (2017)
DOI: 10.1051/0004-6361/201730868

Astronomy & Astrophysics

Asteroid shapes and thermal properties from combined optical and mid-infrared photometry inversion

J. Ďurech[1], M. Delbo'[2], B. Carry[2], J. Hanuš[1], and V. Alí-Lagoa[2,3]

[1] Astronomical Institute, Faculty of Mathematics and Physics, Charles University, V Holešovičkách 2, 180 00 Prague 8, Czech Republic
e-mail: durech@sirrah.troja.mff.cuni.cz
[2] Université Côte d'Azur, Observatoire de la Côte d'Azur, CNRS, Laboratoire Lagrange, 06304 Nice, France
[3] Max-Planck-Institut für extraterrestrische Physik, Giessenbachstraße, Postfach 1312, 85741 Garching, Germany

Received 24 March 2017 / Accepted 1 June 2017

ABSTRACT

Context. Optical light-curves can be used to reconstruct the shape and spin of asteroids. Because the albedo is unknown, these models are scale free. When thermal infrared data are available, they can be used to scale the shape models and derive the thermophysical properties of the surface by applying a thermophysical model.
Aims. We introduce a new method for simultaneously inverting optical and thermal infrared data that allows the size of an asteroid to be derived along with its shape and spin state.
Methods. The method optimizes all relevant parameters (shape and size, spin state, light-scattering properties, thermal inertia, and surface roughness) by gradient-based optimization. The thermal emission is computed by solving the 1D heat diffusion equation. Calibrated optical photometry and thermal fluxes at different wavelengths are needed as input data.
Results. We demonstrate the reliability and test the accuracy of the method on selected targets with different amounts and quality of data. Our results in general agree with those obtained by independent methods.
Conclusions. Combining optical and thermal data into one inversion method opens a new possibility for processing photometry from large optical sky surveys with the data from WISE. It also provides more realistic error estimates of thermophysical parameters.

Key words. minor planets, asteroids: general – radiation mechanisms: thermal – techniques: photometric

1. Introduction

Optical and thermal infrared disk-integrated radiation of asteroids is routinely used for the determination of their physical properties (Kaasalainen et al. 2002; Harris & Lagerros 2002; Ďurech et al. 2015; Delbo et al. 2015, and references therein). The reflected sunlight at optical wavelengths serves as the first guess for the size of the asteroids (from the brightness) and taxonomic type (color information). The periodic variations in brightness that are due to rotation carry information about the shape and spin state of the asteroid. Kaasalainen & Torppa (2001) and Kaasalainen et al. (2001) developed a method for reconstructing the asteroid shape and spin state from disk-integrated reflected light. The method provides reliable results and is mathematically robust, which means it is not sensitive to the noise in data. It has been successfully applied to hundreds of asteroids (Ďurech et al. 2009, 2016a; Hanuš et al. 2011, 2016; Marciniak et al. 2011, for example), and its results were confirmed by independent methods (Kaasalainen et al. 2005; Marchis et al. 2006; Keller et al. 2010; Ďurech et al. 2011). Because the general inverse problem in case of disk-integrated data is ill-posed, the shape is usually modeled as convex. This approach guarantees uniqueness of the model. The output of the light-curve inversion method is a shape model represented by a convex polyhedron that approximates the real nonconvex shape of an asteroid. Because of the ambiguity between size D and geometric albedo p_V, the models are scale free. The visible flux is proportional to $D^2 p_V$ and in principle $0.01 \lesssim p_V \lesssim 1.0$ (Masiero et al. 2011), which means that the size estimation from the visible brightness has a very large uncertainty. The models can be set to scale by disk-resolved data (Hanuš et al. 2013a), stellar occultation silhouettes (Ďurech et al. 2011), or thermal infrared data (Hanuš et al. 2015).

The transition from purely reflected light to purely thermal emission is continuous, and the transition zone where the detected flux is a mixture of reflected solar radiation and thermal emission depends on the heliocentric distance, albedo, and thermal properties of the surface. For asteroids in the main belt it is around 3–5 μm (Delbó & Harris 2002; Harris & Lagerros 2002). For longer wavelengths, the flux can be treated as pure thermal emission. Measurements of this flux can be used for a direct estimation of the size, and sophisticated thermal models have been developed to reveal the thermal properties of the surface from measurements of thermal emission at different wavelengths.

The simplest approach to thermal modeling that is often used when no information about the shape is available is to assume that the shape is a sphere. Then the standard thermal model (STM, Lebofsky et al. 1986) or the near-Earth asteroid thermal model (NEATM, Harris 1998) are used. When interpreting thermal data by a thermophysical model (TPM), the shape and spin state of the asteroid has to be known to be able to compute the viewing and illumination geometry for each facet on the surface (and shadowing in case of a nonconvex model). Usually, the 1D heat diffusion problem is solved in the subsurface layers. There are many different TPM codes, which differ mainly in the way they deal with surface roughness (for a review,

see Delbo et al. 2015). Shape models are usually reconstructed from other data sources such as photometry (Kaasalainen et al. 2002), radar echos (Benner et al. 2015), or high angular resolution imaging (Carry et al. 2010a). Although this approach in general works and provides thermophysical parameters, the main caveat here is that the shape and spin state are taken as a priori assumptions and their uncertainties are not taken into account. This may lead to an underestimation of errors of the derived parameters or even to erroneous results (see Rozitis & Green 2014; Hanuš et al. 2015, for example).

To overcome the limitation of a two-step approach where first the shape and spin model is created and then thermal data are fitted, we have developed a new algorithm that allows for simultaneous optimization of all relevant parameters. We call it convex inversion TPM (CITPM), and we describe the algorithm in Sect. 2 and show how this method works for some test asteroids in Sect. 3.

2. Combined inversion of optical and thermal infrared data

Our new code joins two widely used and well-tested methods: (i) the light-curve inversion of Kaasalainen et al. (2001), and (ii) the thermophysical model of Lagerros (1996, 1997, 1998). We use the convex approach, which enables us to work in the Gaussian image representation: the convex shape is represented by areas of surface facets and corresponding normals. The normals are fixed while the areas are optimized to achieve the best agreement between the visible light and the thermal infrared fluxes calculated by the model and the observed fluxes. Moreover, the distribution of individual areas is parametrized by spherical harmonics (usually on the order and degree of six to eight). The polyhedral representation of the shape is then reconstructed by the Minkowski iteration (Kaasalainen & Torppa 2001). The spin vector is parametrized by the direction of the spin axis in ecliptic coordinates (λ, β) and the sidereal rotation period P. Together with the initial orientation φ_0 at epoch JD_0, these parameters uniquely define the orientation of the asteroid in the ecliptic coordinate frame (Ďurech et al. 2010). With the positions of the Sun and Earth known with respect to the asteroid, the illumination and viewing geometry can be computed for each facet. As we only work with convex shapes, there is no global shadowing by large-scale topography in our model, although the generalization of the problem with nonconvex shapes is straightforward, similar to the case of light-curve inversion.

To compute the brightness of an asteroid in visible light, we use Hapke's model with shadowing (Hapke 1981, 1984, 1986). This model has five parameters: the average particle single-scattering albedo ϖ_0, the asymmetry factor g, the width h and amplitude B_0 of the opposition effect, and the mean surface slope $\bar{\theta}$. We compute Hapke's bidirectional reflectance $r(i, e, \alpha)$ for each surface element, where i is the incidence angle, e is the emission angle, and α is the phase angle. The total flux scattered toward an observer is computed as the sum of contributions from all visible and illuminated facets.

In standard TPM methods, the size of the asteroid D in kilometers and its geometric albedo p_V are connected via the Bond albedo A_B, the phase integral q, and the absolute magnitude H_0 with the formulas (see Harris & Lagerros 2002, for example)

$$D = \frac{1329}{\sqrt{p_\mathrm{V}}}\, 10^{-\frac{H_0}{5}}, \qquad A_\mathrm{B} = q p_\mathrm{V}. \tag{1}$$

However, the Bond albedo A_B as well as the geometric visible albedo p_V are not material properties, and they are unambiguously defined only for a sphere. Instead of this traditional approach, we therefore use a self-consistent model, where the set of Hapke's parameters is also used to compute the total amount of light scattered into the upper hemisphere, which defines the hemispherical albedo A_h (the ratio of power scattered into the upper hemisphere by a unit area of the surface to the collimated power incident on the unit surface area, Hapke 2012) that is needed to compute the energy balance between incoming, emitted, and reflected flux. This hemispherical albedo is dependent on the angle of incidence (it is different for each surface element), and it is at each step computed by numerically evaluating the integral

$$A_\mathrm{h}(i) = \frac{1}{\mu_0} \int_\Omega r(i, e, \alpha)\, \mu \, \mathrm{d}\Omega, \tag{2}$$

where $\mu = \cos e$, $\mu_0 = \cos i$, and the integration region Ω is over the upper hemisphere. Because the above defined quantities are in general dependent on the wavelength λ, we need the bolometric hemispherical albedo A_bol, that is, the average of the wavelength-dependent hemispherical albedo $A_\mathrm{h}(\lambda)$ weighted by the spectral irradiance of the Sun $J_\mathrm{S}(\lambda)$:

$$A_\mathrm{bol} = \frac{\int_0^\infty A_\mathrm{h}(\lambda) J_\mathrm{s}(\lambda)\, \mathrm{d}\lambda}{\int_0^\infty J_\mathrm{s}(\lambda)\, \mathrm{d}\lambda}. \tag{3}$$

In practice, we approximate the integrals by sums. The dependence of A_h on λ is not known from either theory or measurements, therefore we assume that it is the same as the dependence of the physical (geometric) albedo $p(\lambda)$ that can be estimated from reflectance curves. If the asteroid taxonomy is known, we take the spectrum of that class in the Bus-DeMeo taxonomy (DeMeo et al. 2009) and extrapolate the unknown part outside the 0.45–2.45 μm interval with flat reflectance. We then multiply this spectrum by the spectrum of the Sun, taken from Gueymard (2004). If the taxonomic class is unknown, we assume flat reflectance, that is, $A_\mathrm{h}(\lambda) = \mathrm{const}$.

The Bond and geometric albedos can both be computed from Hapke's parameters, but they are not directly used in our model. We do not need the formalism of the HG system either (Bowell et al. 1989). Similar to the geometric albedo, the H_0 value is properly defined only for a sphere; for a real irregular asteroid, it depends on the aspect angle. Instead of using H_0 and p_V, we therefore directly use the calibrated magnitudes on the phase curve. With disk-integrated photometry and a limited coverage of phase angles, it is usually not possible to uniquely determine the Hapke parameters. In such cases, they (or a subset of them) can be fixed at some typical values (see Table 6 of Li et al. 2015).

Parameters of the thermophysical model are the thermal inertia Γ, the fraction of surface covered by craters ρ_c, and their opening angle γ_c (Lagerros 1998). The roughness parameter $\bar{\theta}$ of Hapke's model can be set to the value corresponding to craters or set to a different value, which would mean that there are two values of roughness in the model, one for optical and one for infrared wavelengths. We typically use only one value, which makes the model simpler and also more self-consistent.

To find the best-fitting parameters, we use the Levenberg-Marquardt algorithm. The parameters are optimized to give the lowest value for the total χ^2 that is composed of the visual and infrared part weighted by w:

$$\chi^2_\mathrm{total} = \chi^2_\mathrm{VIS} + w \chi^2_\mathrm{IR}. \tag{4}$$

The visual part is computed as a sum of squares of differences between the observed flux $F_{\mathrm{VIS,\,obs}}$ and the modeled flux $F_{\mathrm{VIS,\,model}}$ over individual data points i weighted by the measurement errors σ_i:

$$\chi^2_{\mathrm{VIS}} = \sum_i \left(\frac{F^{(i)}_{\mathrm{VIS,\,obs}} - F^{(i)}_{\mathrm{VIS,\,model}}}{\sigma_i} \right)^2 . \quad (5)$$

The model flux is computed as a sum over all illuminated and visible surface elements k:

$$F_{\mathrm{VIS,\,model}} = \frac{F_{\mathrm{in}}}{\Delta^2} \sum_k r_k \, \mu_k \, \delta\sigma_k, \quad (6)$$

where F_{in} is the incident solar irradiance, Δ is the distance between the observer and the asteroid, r is Hapke's bidirectional reflectance, μ is the cosine of the emission angle, and $\delta\sigma$ is the area of the surface element. If the photometry is not calibrated and we have only relative light curves, the corresponding χ^2 part is computed such that only the relative fluxes are compared,

$$\chi^2_{\mathrm{rel}} = \sum_j \sum_i \left(\frac{F^{(j)(i)}_{\mathrm{VIS,\,obs}}}{\bar{F}^{(j)}_{\mathrm{VIS,\,obs}}} - \frac{F^{(j)(i)}_{\mathrm{VIS,\,model}}}{\bar{F}^{(j)}_{\mathrm{VIS,\,model}}} \right)^2 , \quad (7)$$

where j is an index for lightcurves, i is an index for individual points of a light curve, and $\bar{F}^{(j)}$ is the mean brightness of the jth light curve.

Similarly, for the IR part of the χ^2 we compute

$$\chi^2_{\mathrm{IR}} = \sum_i \left(\frac{F^{(i)}_{\mathrm{IR,\,obs}} - F^{(i)}_{\mathrm{IR,\,model}}}{\sigma_i} \right)^2 , \quad (8)$$

where we compare the observed thermal flux $F_{\mathrm{IR,\,obs}}$ with the modeled flux $F_{\mathrm{IR,\,model}}$ at some wavelength λ. The disk-integrated flux is a sum of contributions from all surface elements that are visible to the observer:

$$F_{\mathrm{IR,\,model}} = \frac{\epsilon}{\Delta^2} \sum_k B(\lambda, T_k, \rho_{\mathrm{c}}, \gamma_{\mathrm{c}}) \, \mu_k \, \delta\sigma_k, \quad (9)$$

where ϵ is the emissivity (assumed to be independent on λ), and B is radiance of a surface element at temperature T that depends on the wavelength λ (blackbody radiation) and also includes a model for macroscopic roughness parametrized by ρ_{c} and γ_{c}. To compute B, we have to solve the heat diffusion equation for each surface element and compute T_k. Assuming that the material properties do not depend on temperature, we solve

$$\rho C \frac{\partial T}{\partial t} = \kappa \frac{\partial^2 T}{\partial z^2}, \quad (10)$$

where the density ρ, heat capacity C, and thermal conductivity κ are combined into a single parameter thermal inertia $\Gamma = \sqrt{\rho C \kappa}$ (Spencer et al. 1989; Lagerros 1996). Instead of the real subsurface depth z, the problem is then solved in the units of the thermal skin depth, which is related to the rotation period and the thermal properties of the material. The boundary condition at the surface ($z = 0$) is the equation for energy balance:

$$(1 - A_{\mathrm{bol}}) \frac{F_\odot}{r^2} \mu_0 = \epsilon \sigma T^4 - \kappa \frac{\partial T}{\partial z}, \quad (11)$$

where the left side of the equation is the energy absorbed by the surface ($F_\odot$ is solar irradiance at 1 au, r is the distance from the Sun, and μ_0 is the cosine of the incidence angle), and the right side is the radiated flux (σ is the Stefan-Boltzmann constant) minus the heat transported inside the body. The inner boundary condition is

$$\left. \frac{\partial T}{\partial z} \right|_{z \to \infty} = 0, \quad (12)$$

where $z \to \infty$ in practice means a few skin depths. Equation (10) is solved by the simplest explicit method with typically tens of subsurface layers.

The weight w in Eq. (4) is set such that there is a balance between the level of fit to light curves and thermal data. Objectively, the optimum value can be found with the method proposed by Kaasalainen (2011) with the so-called maximum compatibility estimate, which corresponds to the maximum likelihood or maximum a posteriori estimates in the case of a single data mode.

Because the correlation between the thermal inertia Γ and the surface roughness is strong, the parameters describing the surface fraction covered by craters ρ_{c} and their opening angle γ_{c} and likewise the parameter $\bar{\theta}$ in Hapke's model are the only three parameters that are not optimized. They are held fixed, and their best values are found by running the optimization many times with different combination of these parameters. The dependence of χ^2_{total} on Γ usually shows only one minimum (sharp or shallow depending on the amount and quality of thermal data), which makes convergence in Γ robust, and the gradient-based optimization converges to the best value of Γ even when it started far from it. The emissivity ϵ is held fixed. Its value can be set to anything between 0 and 1, but in all tests in the following section we used the "standard" value $\epsilon = 0.9$. This is a typical value of the emissivity of meteorites and of the minerals included in meteorites obtained in the laboratory at wavelengths around 10 μm. This value can change significantly at longer wavelengths, see Delbo et al. (2015) for a discussion.

3. Testing the method on selected targets

We tested our method on selected targets, each representing a typical amount of data. First, we used asteroid (21) Lutetia, for which a wealth of photometry and thermal infrared data are available and the shape is known from Rosetta spacecraft flyby. This makes it an ideal target for comparing the results from our inversion with ground truth from Rosetta. Another test asteroid with known shape is (2867) Šteins, but in this case, thermal data are scarce, so that this example should show us the limits of the method. Then we have selected asteroid (306) Unitas – a typical example of an asteroid with enough light curves and some thermal data from IRAS and WISE satellites. As the last example, we show on asteroid (220) Stephania how thermal data in combination with sparse optical photometry can lead to a unique model – this is perhaps the most important aspect of the new method that can lead to production of new asteroid models in the future.

3.1. Data

The success of the method is based on the assumption that we have accurately calibrated absolute photometry of an asteroid covering a wide interval of phase angles – to be able to use Hapke's photometric model and derive the hemispherical albedo. Because most of the available light curves are only relative, we also used the Lowell Observatory photometric database (Oszkiewicz et al. 2011; Bowell et al. 2014) as the source of absolutely calibrated photometry in the V filter. The only asteroid

Table 1. Number of dense light curves N_{lc}, sparse data points N_{sp}, and IRAS and WISE observations.

Asteroid	N_{lc}	N_{sp}	IRAS				WISE		reduced χ^2_{IR}
			12 μm	25 μm	60 μm	100 μm	11 μm	22 μm	
21 Lutetia[a]	59		5	5	5	9			0.80
220 Stephania		397	2	2	2		11	11	0.58
306 Unitas	15	386	11	11	11		10	13	0.68
2867 Šteins	21	614					12	12	0.77

Notes. The goodness of fit to the thermal data is expressed by the reduced χ^2_{IR}. [(a)] For Lutetia, we did not use sparse data because 20 of the set of 59 dense light curves were calibrated. The IR data set also contained data from the *Spitzer* and *Herschel* telescopes.

Table 2. Comparison between our CITPM models and independent results.

Asteroid	λ [deg]	β [deg]	D [km]	p_V	Γ J m^{-2} s$^{-0.5}$ K^{-1}	References
21 Lutetia	56	−7	101 ± 4	0.19–0.23	30–60	CITPM (3σ errors)
	52.2 ± 0.4	−7.8 ± 0.4	98 ± 2	0.19 ± 0.01		Sierks et al. (2011)
			95.97		<10	O'Rourke et al. (2012)
					<30	Keihm et al. (2012)
			98.3 ± 5.9	0.208 ± 0.025	<100	Mueller et al. (2006)
220 Stephania	24 (or 224)	−60 (or −59)	32–34	0.075 ± 0.015	5–75	CITPM
	26 (or 223)	−50 (or −62)				Hanuš et al. (2013b)
			31.738 ± 0.219	0.069 ± 0.016		Masiero et al. (2014)
306 Unitas	82	−30	48.7 ± 0.7	0.21–0.27	10–100	CITPM
	79	−35	49 ± 5			Ďurech et al. (2007, 2011)
			55–56	0.14–0.15	100–260	Delbo & Tanga (2009)
			47.2 ± 0.13	0.201 ± 0.013		Masiero et al. (2014)
2867 Šteins	142	−83	5.6–6.2	0.4–0.5	70–370	CITPM
	94	−85 ± 5	5.26 ± 0.26			Jorda et al. (2012)
				0.39 ± 0.02		Spjuth et al. (2012)
					210 ± 30	Leyrat et al. (2011)

Notes. The physical parameters are the ecliptic longitude λ and latitude β of the spin axis direction, the volume-equivalent diameter D, the geometric albedo p_V, and the thermal inertia of the surface Γ.

for which we had enough reliable absolutely calibrated dense light curves was (21) Lutetia. For the thermal data, we used the IRAS catalog (Tedesco et al. 2004), WISE data (Wright et al. 2010; Mainzer et al. 2011), and also *Spitzer* and *Herschel* observations for (21) Lutetia. The number of dense light curves (usually relative), sparse data points (calibrated), and IR data points for all targets is listed in Table 1. The comparison between CITPM models and independent models is shown in Table 2 in terms of derived physical parameters.

3.2. (21) Lutetia

Because for this asteroid many light curves define the convex shape well, we do not expect any significant improvement of the model with respect to the two-step method. However, Lutetia with its abundant photometric and infrared data set is a good test case for the new algorithm.

A convex model of Lutetia was derived by Torppa et al. (2003), and Carry et al. (2010b) later created a nonconvex model that was confirmed by the Rosetta fly-by (Carry et al. 2012). The detailed shape model of Lutetia reconstructed from the fly-by imaging (Sierks et al. 2011) can serve as a ground-truth comparison with our model (although part of the surface was not seen by Rosetta and was reconstructed from light curves). There are also abundant optical and thermal infrared data for this asteroid – 59 light curves observed between 1962 and 2010, out of which 20 are calibrated in V filter, and thermal infrared data (O'Rourke et al. 2012) from 7.87 (*Spitzer*) to 160 μm (*Herschel* PACS). We did not include the *Herschel* SPIRE data observed at 250, 350, and 500 μm because at these long wavelengths the emissivity assumption of $\epsilon = 0.9$ is no longer valid (see the discussion in Delbo et al. 2015, for example).

The comparison between our model reconstructed from disk-integrated light curves and thermal data and the model reconstructed by Sierks et al. (2011) from Rosetta fly-by images is shown in Fig. 1. The volume-equivalent diameter of the Rosetta-based model is 98 ± 2 km, while our model has a diameter of 101 ± 4 km. Our thermal inertia of 30–50 J m^{-2} s$^{-0.5}$ K^{-1} is significantly higher than the value ~5 J m^{-2} s$^{-0.5}$ K^{-1} of O'Rourke et al. (2012), at the boundary of interval <30 J m^{-2} s$^{-0.5}$ K^{-1} given by Keihm et al. (2012), and consistent with the value of ≤100 J m^{-2} s$^{-0.5}$ K^{-1} of

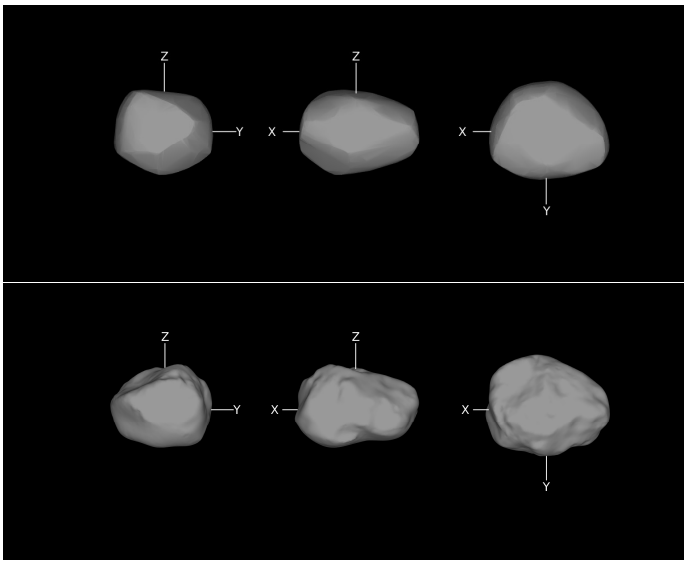

Fig. 1. Comparison between the shape of (21) Lutetia reconstructed by our method (*top*) and that reconstructed by Sierks et al. (2011) from Rosetta fly-by images (*bottom*).

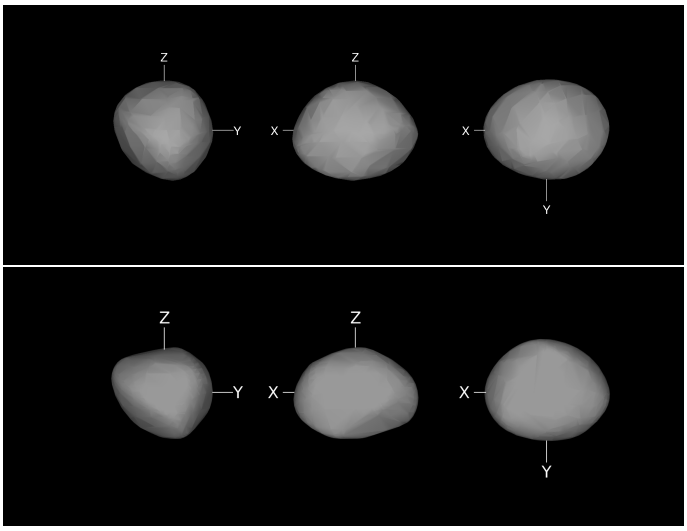

Fig. 2. Comparison between the new shape of (306) Unitas reconstructed from thermal and optical data (*top*) and that reconstructed from only dense optical light-curves by Ďurech et al. (2007; *bottom*).

Mueller et al. (2006) derived from IRAS and IRTF (InfraRed Telescope Facility) data. The discrepancy between our values and those by O'Rourke et al. (2012) and Keihm et al. (2012) might partly be caused by the fact that we used only wavelengths $\leq$160 μm, while the lower values of thermal inertia were derived from data sets that also contained submillimeter and millimeter wavelengths. Longer wavelengths "see" deeper in the subsurface, which is colder than the surface layers. Since Γ depends on the temperature, we expect to see Γ decreasing with depth, provided the density and packing of the regolith is independent of the depth, which might not be the case. For example, on the Moon the regolith density increases with depth (Vasavada et al. 2012). Harris & Drube (2016) claimed to see the same effect on asteroids.

3.3. (306) Unitas

Unitas is a typical example of a main-belt asteroid for which there are some data from both IRAS and WISE (see Table 1). The first convex model was published by Ďurech et al. (2007) with a pole ambiguity that was later resolved with IR data by Delbo & Tanga (2009) and confirmed with a fit to stellar occultation data by Ďurech et al. (2011). The new CITPM shape model obtained from a combined inversion of optical light-curves and thermal data has a pole direction of $(\lambda, \beta) = (82°, -30°)$ and a shape similar (Fig. 2) to the old model with a pole direction of (79°, −35°). The size of the formally best-fitting model (derived independently of the occultation) is 48.7 ± 0.7 km, which is very close to the size 49 ± 5 km obtained by scaling the light-curve-based model to occultation chords. For comparison, the size estimated from the IRAS observation is 46.7±2.3 km (Tedesco et al. 2004), from WISE it is 51.6 ± 6.3 km (Masiero et al. 2011), and from AKARI it is 46.2 ± 0.6 km (Usui et al. 2011).

The comparison between the model silhouette and the fit to the occultation is shown in Fig. 3, where the red contour corresponds to our new model (no scaling, rms residual 1.7 km) and the blue contour corresponds to the model of Ďurech et al. (2007) that was scaled to provide the best fit to the chords (rms residual 1.9 km). The fit between the model and observations is formally

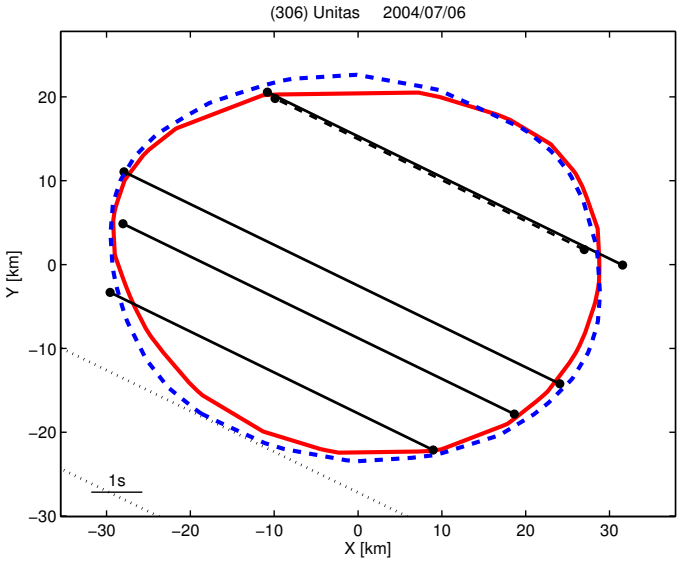

Fig. 3. Plane-of-the-sky silhouettes of (306) Unitas for the time of the occultation. The red solid silhouette corresponds to our model, the blue dashed silhouette corresponds to the model from Ďurech et al. (2007). The black lines represent chords reconstructed from timings and positions of individual observers. The dashed chord represents a visual observation with uncertain timing, the dotted lines are a negative observations with no occultation detected. Occultation data were taken form Dunham et al. (2016).

very good (Fig. 4) with a reduced $\chi^2_{\rm IR}$ as low as ~0.7 for thermal inertia in the range 10–100 J m^{-2} s$^{-0.5}$ K^{-1}. Delbo & Tanga (2009) applied TPM on only IRAS data and derived systematically higher thermal inertia 100–260 J m^{-2} s$^{-0.5}$ K^{-1} and also a size of 55–56 km – this demonstrates that with a fixed shape and spin as an input for TPM, the uncertainties of the thermophysical parameters are often underestimated (see also Hanuš et al. 2015).

As can be seen in Fig. 2, adding IR data changed the shape model only slightly, but the data allowed correct scaling of the size, which can be independently checked by the occultation in Fig. 3.

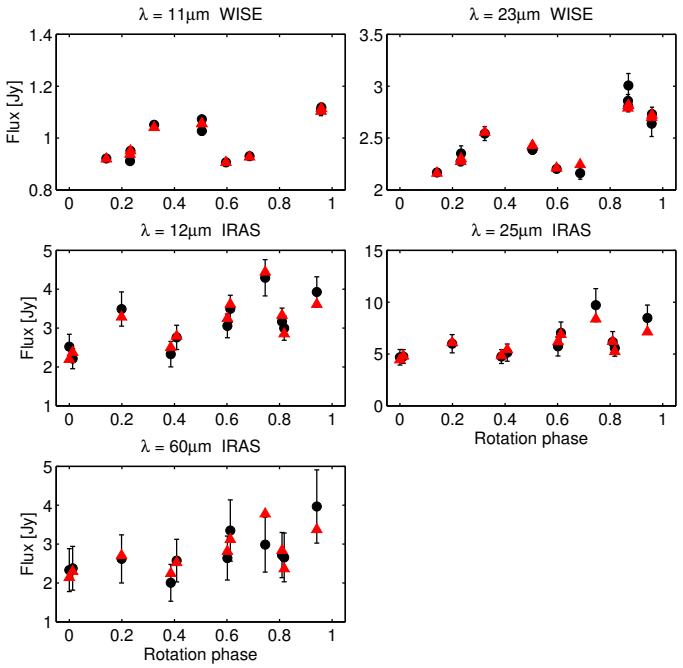

Fig. 4. Measured IR fluxes (black circles) of (306) Unitas and the model fluxes for our model (red triangles).

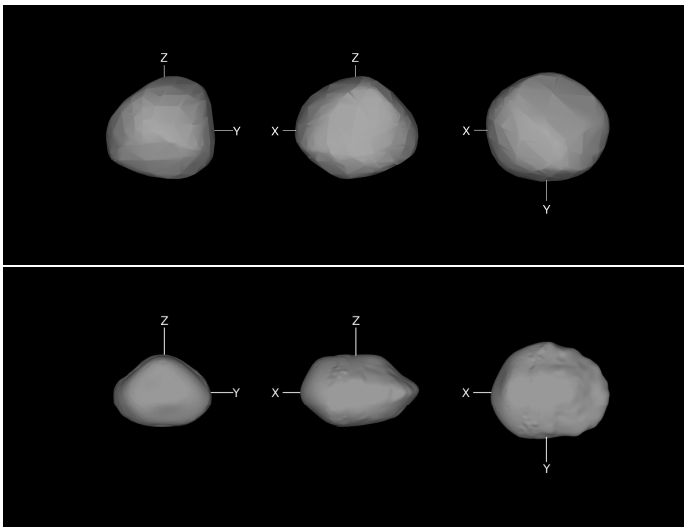

Fig. 5. Comparison between the shape of (2867) Šteins reconstructed with our method (*top*) and that reconstructed by Jorda et al. (2012) from Rosetta fly-by images and light curves (*bottom*).

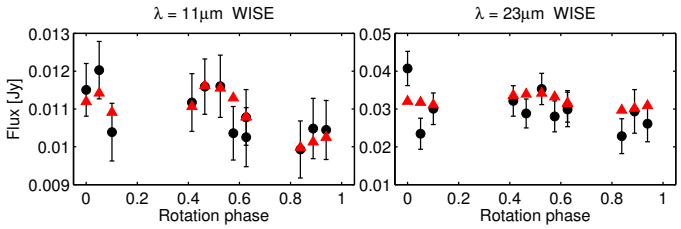

Fig. 6. Measured IR fluxes (black circles) of (2867) Šteins and the model fluxes for our model (red triangles).

3.4. (2867) Šteins

Similarly to Lutetia, for this asteroid we also have a detailed reconstructed shape model from the Rosetta fly-by images and light curves (Jorda et al. 2012). In contrast to Lutetia, however, thermal data for Šteins are limited to only twelve pairs of WISE data with a relative accuracy of 7% and 15% in the W3 and W4 filter, respectively. Therefore the thermal properties are poorly constrained. Models with a diameter in the range 5.6–6.2 km and a thermal inertia 70–370 J m^{-2} s$^{-0.5}$ K^{-1} provide an acceptable fit to both thermal and optical data. There is a correlation between these two parameters – solutions with a smaller diameter have also a lower thermal inertia. The geometric visible albedo is in the range 0.4–0.5. One of the possible shape models is shown in Fig. 5, and the fit to the thermal data is presented in Fig. 6. The selected model has an equivalent diameter of 5.8 km and a thermal inertia of 200 J m^{-2} s$^{-0.5}$ K^{-1}. For comparison, the shape reconstructed from Rosetta images and light curves has an equivalent diameter of 5.26 ± 0.26 km (Jorda et al. 2012). The main difference between the CITPM model and that of Jorda et al. (2012) is that the Rosetta-based model is much flatter than the CITPM model, which might also be the reason why our model has a larger equivalent diameter. Leyrat et al. (2011) derived from VIRTIS/Rosetta measurements the thermal inertia $\Gamma = 110 \pm 13$ J m^{-2} s$^{-0.5}$ K^{-1} for a smooth surface and $\Gamma = 210 \pm 30$ J m^{-2} s$^{-0.5}$ K^{-1} when a small-scale roughness was included. Spjuth et al. (2012) determined a geometric albedo of 0.39 ± 0.02 at 670 nm from disk-resolved photometry. This shows that a combined inversion is still possible with low-quality thermal data, but the derived physical parameters have large uncertainties.

3.5. (220) Stephania

As the last example we selected an asteroid for which optical data are not sufficient to derive a unique model. To demonstrate the potential of combining sparse photometry with WISE data, we selected asteroid (220) Stephania, which was modeled by Hanuš et al. (2013b) from a set of nine light curves and sparse data from the US Naval Observatory and the Catalina Sky Survey. The pole direction was (26°, −50°) or (223, −62°). Here we use only Lowell sparse photometry and WISE data in W1 (8 points) and W2 (7 points) to determine the period with the light curve inversion method of Kaasalainen et al. (2001). As is shown in Fig. 7, sparse data alone are not sufficient to determine the rotation period uniquely. In the periodogram, there are many possible periods (and corresponding models) that provide the same level of fit for the data. However, when we add WISE data from W1 and W2 filters and assume that they can be treated as reflected light (Ďurech et al. 2016b), the correct period of about 18.2 h now gives the global minimum in the periodogram. Even though there are fewer WISE data points than were available in the Lowell data (~400 points), they were observed within an interval of one day and their contribution to constraining the period is significant. Then, this period is used as a start point for the CITPM model that now combines only Lowell photometry, WISE thermal data in the W3 and W4 filters, and IRAS data. The best model has pole directions (24°, −60°) or (224°, −59°) and thermophysical parameters $\Gamma = 15^{+60}_{-10}$ J m^{-2} s$^{-0.5}$ K^{-1}, $D = 32.2^{+2.0}_{-0.2}$ km, and $p_V = 0.075 \pm 0.15$. The fit to the IRAS and WISE thermal data is shown in Fig. 8. The rotation phase shift between the optical and thermal light curves is very small, only about 10°, which justifies the use of thermal data for the period determination.

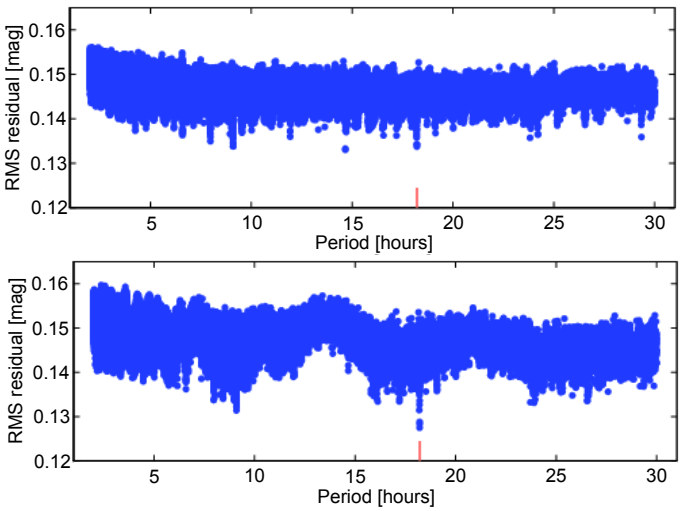

Fig. 7. Period search for (220) Stephania for Lowell photometry (*top*) and Lowell + WISE W1 and W2 data (*bottom*). The correct rotation period of 18.2 h is marked with a red tick.

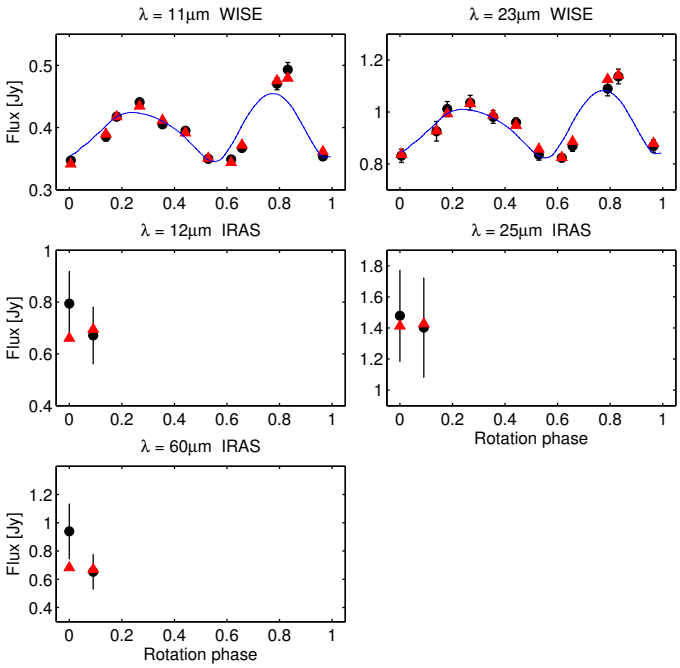

Fig. 8. Measured IR fluxes (black circles) of (220) Stephania and the model fluxes for our model (red triangles). The WISE data are shown together with the synthetic optical light-curve (blue) produced by the model.

4. Conclusions and future work

The new approach of a combined inversion of thermal and optical data opens a new possibility of analyzing IR data and visual photometry for tens of thousands of asteroids for which both data modes are available. As a first step, we will apply this method to asteroids for which a shape model exists in the DAMIT database (Ďurech et al. 2010) and for which there are WISE or IRAS data, with the aim to derive complete physical models.

As the next step, WISE data can be processed together with the sparse photometric data with the aim to derive unique models in cases when neither visual photometry nor thermal data are sufficient alone. Because WISE data constrain the rotation period and Lowell photometry covers various geometries, we expect that thousands of new models can be derived from these data sets.

Acknowledgements. The work of J.Ď. was supported by the grant 15-04816S of the Czech Science Foundation. B.C. acknowledges the support of the ESAC Science Faculty for J.Ď. visit. V.A.L. has received funding from the European Union's Horizon 2020 Research and Innovation Programme, under Grant Agreement No. 687378. V.A.L. and M.D. acknowledge support from the NEOShield-2 project, which has received funding from the European Union's Horizon 2020 research and innovation programme under grant agreement No. 640351. This publication also makes use of data products from NEOWISE, which is a project of the Jet Propulsion Laboratory/California Institute of Technology, funded by the Planetary Science Division of the National Aeronautics and Space Administration.

References

Benner, L. A. M., Busch, M. W., Giorgini, J. D., Taylor, P. A., & Margot, J.-L. 2015, in Asteroids IV, eds. P. Michel, F. E. DeMeo, & W. F. Bottke (Tucson: University of Arizona Press), 165
Bowell, E., Hapke, B., Domingue, D., et al. 1989, in Asteroids II, eds. R. P. Binzel, T. Gehrels, & M. S. Matthews (Tucson: University of Arizona Press), 524
Bowell, E., Oszkiewicz, D. A., Wasserman, L. H., et al. 2014, Meteoritics and Planetary Science, 49, 95
Carry, B., Dumas, C., Kaasalainen, M., et al. 2010a, Icarus, 205, 460
Carry, B., Kaasalainen, M., Leyrat, C., et al. 2010b, A&A, 523, A94
Carry, B., Kaasalainen, M., Merline, W. J., et al. 2012, Planet. Space Sci., 66, 200
Delbó, M., & Harris, A. W. 2002, Meteoritics, 37, 1929
Delbo, M., & Tanga, P. 2009, Planet. Space Sci., 57, 259
Delbo, M., Mueller, M., Emery, J. P., Rozitis, B., & Capria, M. T. 2015, in Asteroids IV, eds. P. Michel, F. E. DeMeo, & W. F. Bottke (Tucson: University of Arizona Press), 107
DeMeo, F. E., Binzel, R. P., Slivan, S. M., & Bus, S. J. 2009, Icarus, 202, 160
Dunham, D. W., Herald, D., Frappa, E., et al. 2016, NASA Planetary Data System, 243
Ďurech, J., Scheirich, P., Kaasalainen, M., et al. 2007, in Near Earth Objects, our Celestial Neighbors: Opportunity and Risk, eds. A. Milani, G. B. Valsecchi, & D. Vokrouhlický (Cambridge: Cambridge University Press), 191
Ďurech, J., Kaasalainen, M., Warner, B. D., et al. 2009, A&A, 493, 291
Ďurech, J., Sidorin, V., & Kaasalainen, M. 2010, A&A, 513, A46
Ďurech, J., Kaasalainen, M., Herald, D., et al. 2011, Icarus, 214, 652
Ďurech, J., Carry, B., Delbo, M., Kaasalainen, M., & Viikinkoski, M. 2015, in Asteroids IV, eds. P. Michel, F. E. DeMeo, & W. F. Bottke (Tucson: University of Arizona Press), 183
Ďurech, J., Hanuš, J., Oszkiewicz, D., & Vančo, R. 2016a, A&A, 587, A48
Ďurech, J., Hanuš, J., Alí-Lagoa, V. M., Delbo, M., & Oszkiewicz, D. A. 2016b, IAU Symp., 318, eds. S. R. Chesley, A. Morbidelli, R. Jedicke, & D. Farnocchia, 170
Gueymard, C. A. 2004, Solar Energy, 76, 423
Hanuš, J., Ďurech, J., Brož, M., et al. 2011, A&A, 530, A134
Hanuš, J., Marchis, F., & Ďurech, J. 2013a, Icarus, 226, 1045
Hanuš, J., Ďurech, J., Brož, M., et al. 2013b, A&A, 551, A67
Hanuš, J., Delbo, M., Ďurech, J., & Alí-Lagoa, V. 2015, Icarus, 256, 101
Hanuš, J., Ďurech, J., Oszkiewicz, D. A., et al. 2016, A&A, 586, A108
Hapke, B. 1981, J. Geophys. Res., 86, 3039
Hapke, B. 1984, Icarus, 59, 41
Hapke, B. 1986, Icarus, 67, 264
Hapke, B. 2012, Theory of Reflectance and Emittance Spectroscopy (Cambridge University Press)
Harris, A. W. 1998, Icarus, 131, 291
Harris, A. W., & Drube, L. 2016, ApJ, 832, 127
Harris, A. W., & Lagerros, J. S. V. 2002, in Asteroids III, eds. W. F. Bottke, A. Cellino, P. Paolicchi, & R. P. Binzel (Tucson: University of Arizona Press), 205
Jorda, L., Lamy, P. L., Gaskell, R. W., et al. 2012, Icarus, 221, 1089
Kaasalainen, M. 2011, Inverse Problems and Imaging, 5, 37
Kaasalainen, M., & Torppa, J. 2001, Icarus, 153, 24
Kaasalainen, M., Torppa, J., & Muinonen, K. 2001, Icarus, 153, 37

Kaasalainen, M., Mottola, S., & Fulchignomi, M. 2002, in Asteroids III, eds. W. F. Bottke, A. Cellino, P. Paolicchi, & R. P. Binzel (Tucson: University of Arizona Press), 139
Kaasalainen, M., Hestroffer, D., & Tanga, P. 2005, in The Three-Dimensional Universe with Gaia, ESA SP, 576, 301
Keihm, S., Tosi, F., Kamp, L., et al. 2012, Icarus, 221, 395
Keller, H. U., Barbieri, C., Koschny, D., et al. 2010, Science, 327, 190
Lagerros, J. S. V. 1996, A&A, 310, 1011
Lagerros, J. S. V. 1997, A&A, 325, 1226
Lagerros, J. S. V. 1998, A&A, 332, 1123
Lebofsky, L. A., Sykes, M. V., Tedesco, E. F., et al. 1986, Icarus, 68, 239
Leyrat, C., Coradini, A., Erard, S., et al. 2011, A&A, 531, A168
Li, J.-Y., Helfenstein, P., Burrati, B. J., Takir, D., & Clark, B. E. 2015, in Asteroids IV, eds. P. Michel, F. E. DeMeo, & W. F. Bottke (Tucson: University of Arizona Press), 129
Mainzer, A., Bauer, J., Grav, T., et al. 2011, ApJ, 731, 53
Marchis, F., Kaasalainen, M., Hom, E. F. Y., et al. 2006, Icarus, 185, 39
Marciniak, A., Michałowski, T., Polińska, M., et al. 2011, A&A, 529, A107
Masiero, J. R., Mainzer, A. K., Grav, T., et al. 2011, ApJ, 741, 68
Masiero, J. R., Grav, T., Mainzer, A. K., et al. 2014, ApJ, 791, 121
Mueller, M., Harris, A. W., Bus, S. J., et al. 2006, A&A, 447, 1153
O'Rourke, L., Müller, T., Valtchanov, I., et al. 2012, Planet. Space Sci., 66, 192
Oszkiewicz, D., Muinonen, K., Bowell, E., et al. 2011, J. Quant. Spectr. Rad. Transf., 112, 1919
Rozitis, B., & Green, S. F. 2014, A&A, 568, A43
Sierks, H., Lamy, P., Barbieri, C., et al. 2011, Science, 334, 487
Spencer, J. R., Lebofsky, L. A., & Sykes, M. V. 1989, Icarus, 78, 337
Spjuth, S., Jorda, L., Lamy, P. L., Keller, H. U., & Li, J.-Y. 2012, Icarus, 221, 1101
Tedesco, E. F., Noah, P. V., Noah, M., & Price, S. D. 2004, NASA Planetary Data System, 12
Torppa, J., Kaasalainen, M., Michalowski, T., et al. 2003, Icarus, 164, 346
Usui, F., Kuroda, D., Müller, T. G., et al. 2011, PASJ, 63, 1117
Vasavada, A. R., Bandfield, J. L., Greenhagen, B. T., et al. 2012, J. Geophys. Res. (Planets), 117, E00H18
Wright, E. L., Eisenhardt, P. R. M., Mainzer, A. K., et al. 2010, AJ, 140, 1868